DEVELOPMENT OF LINEAR ELASTIC AND ELASTOPLASTIC FINITE ELEMENT SOLVERS FOR FORGING SIMULATION

Qi Liu, BaoQi Guo, MingZe Zhang, ZhaoChen Ma, WangZhe Du, Tao Wang – College of Mechanical Engineering, Taiyuan University of Technology, Taiyuan 030024, China

Forging simulations must accommodate large deformation, material nonlinearity, and persistent billet-die contact. This work develops linear-elastic and elastoplastic explicit finite element solvers for bulk-metal forming. The formulation combines lumped-mass discretization and central-difference time integration within a single time-marching loop that updates element kinematics, constitutive response, stresses and history variables, internal, external and contact forces, friction, and nodal motion; stability is controlled by the critical time step. A three-level verification strategy is adopted. In linear-elastic compression, the final axial-stress error is 0.050%, the mean path error is 0.034%, and the final reaction-force error is 2.688%. In elastoplastic compression, the final stress error is 0.019% and the final equivalent-plastic-strain error is 0.569%. For cylindrical upsetting with a 30% reduction, the errors in maximum diameter, final height, and peak load are approximately 0.54%, 0.10%, and 0.91%, respectively, with a mean load-path error of 1.07%. A radial ring-rolling case is then used to examine moving contact under main-roll rotation and continuous mandrel feed. The solver reproduces continuous ring expansion from bite-in to final forming and the migration of high von Mises stress regions with the contact zones. The results demonstrate consistent numerical accuracy across basic response, material nonlinearity, and contact forming, supporting further application to forging and ring-rolling mechanics.

KEYWORDS: EXPLICIT FINITE ELEMENT METHOD – FORGING – ELASTOPLASTICITY – CONTACT – CYLINDRICAL UPSETTING – RADIAL RING ROLLING

INTRODUCTION

Forging is widely used to manufacture large, high-performance metallic components. Material flow is governed simultaneously by geometric constraints, plastic hardening, contact friction, and the loading path. Finite element analysis can continuously provide displacement, stress, plastic strain, and forming-load information that is difficult to measure comprehensively in experiments, and has therefore become an important tool for die-forging defect prediction, deformation analysis of large forgings, and process optimization [1]-[4]. As component size and process complexity increase, a solver must not only represent material nonlinearity but also robustly handle continuously evolving billet-die contact. Interfacial friction directly affects surface slip, barreling, and the overall forming load [5].

For bulk-forming problems involving large deformation, strong material nonlinearity, and complex contact, explicit time integration updates acceleration, velocity, and displacement directly from a diagonalized mass matrix and the current resultant nodal force. It therefore avoids constructing and iteratively solving a global tangent system within every time increment and is well suited to processes with rapidly changing contact conditions [6]. The method is conditionally stable, however, and the allowable time step is constrained by the smallest element dimension and the material wave speed. When explicit dynamics is used to represent a quasi-static forming process, the loading history must also be selected so that inertial effects remain sufficiently small.

Many existing forging studies rely on mature commercial software to investigate materials, processes, and defects [1]-[4][7][8], whereas publicly reported work that verifies basic discretization, constitutive updating, and contact-forming response in a layered solver-oriented manner is comparatively limited. Assessment based only on contour similarity in a single complex case makes it difficult to distinguish errors arising from the element formulation, constitutive integration, or contact treatment. Accordingly, this study constructs a unified explicit finite element framework and adopts a progressive verification strategy from linear elasticity to elastoplasticity and finally to contact forming. Analytical relations are first used to verify the basic mechanical loop; yield and plastic-history evolution are then examined; and frictional upsetting is used to assess the deformation profile and load transfer. Section 4 further considers radial ring rolling, where continuous moving contact is produced by main-roll rotation and mandrel feed, to examine ring expansion, wall-thickness reduction, and the evolution of von Mises equivalent stress under a more complex curved-contact condition.

EXPLICIT FINITE ELEMENT THEORY AND SOLUTION PROCEDURE

Governing equations and time integration

After finite element spatial discretization, the semi-discrete equation of motion at time t_n is written as

$$Ma_n = F_n^{ext} + F_n^{cont} + F_n^{\text{int}} \qquad [1]$$

where M is the mass matrix, a_n is the nodal acceleration, and F_n^{ext}, F_n^{cont}, and F_n^{int} are the external, contact, and internal force vectors, respectively. A lumped-mass discretization is adopted, so the mass matrix is diagonal and the nodal acceleration can be obtained directly from the current resultant force. Velocity is defined at half time steps and displacement at integer time steps; the central-difference updates are

$$v_{n+\frac{1}{2}} = v_{n-\frac{1}{2}} + \Delta t_n a_n \qquad [2]$$

$$u_{n+1} = u_n + \Delta t_{n+\frac{1}{2}} v_{n+\frac{1}{2}} \qquad [3]$$

After the nodal coordinates are updated, the solution advances to element kinematics and contact detection for the next time step. Each step sequentially evaluates the element deformation increment, constitutive response, stresses and history variables, element internal force, external and contact forces, nodal acceleration, and finally the velocity and displacement. The complete solution sequence is shown in Fig. 1.

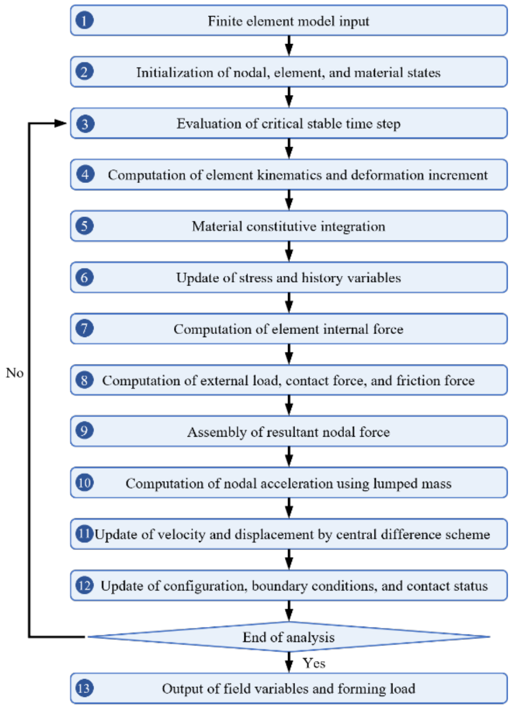

Fig.1 - Overall computational flow of the explicit finite element solver

Linear-elastic and elastoplastic constitutive models

The linear-elastic stage adopts the isotropic Hooke law, $\sigma = \mathbb{C}(E, \nu) : \varepsilon^e$. No yield check or plastic-history variable is involved at this level, allowing the effects of material nonlinearity to be separated from element kinematics, lumped mass, constraint enforcement, and explicit time marching. It therefore serves as the basic verification level of the complete solution framework.

The elastoplastic stage adopts the von Mises yield criterion, with equivalent plastic strain used as the hardening-history variable:

$$f\left(\sigma, \bar{\varepsilon}^p\right) = \sigma_{eq} - \sigma_y\left(\bar{\varepsilon}^p\right) \leq 0, \sigma_{eq} = \sqrt{\frac{3}{2} S : S} \qquad [4]$$

At each time step, an elastic trial stress is first constructed. If the trial state remains inside the yield surface, an elastic update is performed. If the yield function is activated, a plastic correction is carried out and $\bar{\varepsilon}^p$ together with the associated history variables is updated. The updated stress immediately contributes to the current internal-force calculation; material plasticity therefore influences the subsequent motion directly through the nodal force balance, providing consistent coupling between constitutive integration and explicit time advancement.

Contact, friction, and stable time step

Penalty-based normal contact is used between the billet and the dies. When a normal penetration δ_n is detected, the contact restoring force is $F_n = k_p \delta_n$, where k_p is the penalty stiffness; the tangential response follows the Coulomb condition $|F_t| \leq \mu |F_n|$. The penalty formulation introduces no additional contact degrees of freedom and is well suited to explicit calculation. An excessively large penalty stiffness reduces the allowable time step, whereas an excessively small value increases numerical penetration; a balance is therefore required between contact accuracy and stability [9][10].

The stability scale of the central-difference scheme is approximated by $\Delta t_{\mathrm{cr}} \approx \frac{L_c}{c}$, where L_c is the characteristic element length and c is the characteristic material wave speed. The solution is advanced using the minimum stable time scale in the model, which is updated as mesh distortion and material state evolve. For quasi-static forming, the kinetic- and internal-energy histories are also examined to confirm that the chosen loading rate does not cause inertial response to dominate the principal forming process.

DEVELOPMENT OF THE EXPLICIT FINITE ELEMENT SOLVER FOR FORGING

The solver is organized around a unified explicit main loop. Linear-elastic and elastoplastic analyses share the same mesh discretization, nodal masses, force balance, boundary-condition treatment, contact detection, and time integration; they differ only in the constitutive relation used for integration-point material updates. At the start of an analysis, nodal, elemental, material, boundary, and contact data are read, nodal motion states and integration-point history variables are initialized, and the initial stable time step is evaluated. The solver then performs element kinematics, constitutive updating, internal-force evaluation, contact and external-force calculation, resultant nodal-force assembly, and central-difference motion updating until the prescribed analysis time or die stroke is reached.

This organization keeps the material state, contact state, and geometric configuration synchronized on a single time line. The linear-elastic level verifies the basic finite element discretization; the elastoplastic level adds yielding and hardening without changing the main loop; and the forging-analysis level further introduces rigid-die motion, penalty contact, and friction. During forming, the solver outputs displacement, stress, equivalent plastic strain, contact state, and die reaction force, from which the load-stroke history is constructed. Field variables and reaction forces are recorded at a common output frequency so that local material states and global forming loads can be compared at identical times. The quantitative verification in this paper focuses on the mechanical solution chain. Temperature-related input may be retained in the ring-rolling application case, but no thermal-field accuracy claim is made here. Remeshing, systematic thermo-mechanical coupling verification, and parallel computation, which has also been explored for forming simulation [11], are treated as future extensions.

NUMERICAL VERIFICATION

A three-level verification program is used to isolate different error sources. The linear-elastic case examines element discretization, lumped mass, internal-force evaluation, and time integration; the elastoplastic case examines yielding, hardening-path response, and plastic-history evolution; and the cylindrical-upsetting case jointly examines plastic flow, contact, friction, and forming load. All comparisons use consistent geometry, material parameters, and boundary conditions, with analytical solutions or reference finite element results serving as independent benchmarks. Cylindrical compression/upsetting is also widely used as a benchmark configuration for assessing metal-forming simulations [12].

Linear-elastic solver verification

The linear-elastic verification uses a cylindrical specimen 20 mm in diameter and 30 mm in height, with material parameters $E=210$ GPa and $v=0.3$. The upper and lower dies are treated as rigid boundaries and interfacial friction is set to zero to obtain an approximately uniform uniaxial compression state. The upper die moves at 3 mm/s, and the total compression is approximately 0.03 mm, corresponding to a final engineering strain of about 0.10%. Fig. 2 shows the model, axial stress-strain curve, and reaction-force-displacement response.

The analytical axial stress at the final state is 208.95 MPa, whereas the developed solver gives 209.06 MPa, corresponding to a final relative error of 0.050% and a mean path error of 0.034%. The theoretical final reaction force is 65.64 kN and the solver result is 63.88 kN, giving a final error of 2.688% and a mean path error of 2.493%. The stress path is almost coincident with the analytical solution, indicating close consistency among the element kinematics, constitutive update, and explicit time integration. The somewhat larger reaction-force error is plausibly associated with cumulative discretization effects from the tetrahedral mesh and the transfer of contact reactions to the global boundary. During the principal loading stage, the kinetic-to-internal-energy ratio remains low, and no appreciable inertial contamination of the quasi-static response is observed.

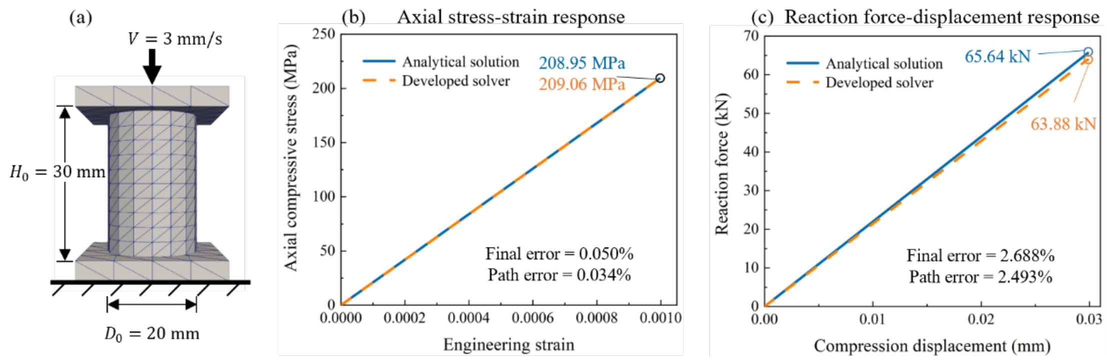

Fig.2 - Linear-elastic compression model and comparison of axial stress and reaction-force responses

Elastoplastic solver verification

The elastoplastic verification uses the same geometry with a refined tetrahedral mesh containing 10,080 TETRA4 elements. The elastic parameters remain $E = 210$ Gpa and $\nu = 0.3$, the initial yield stress is 250 MPa, and linear isotropic hardening is defined by $\sigma_y = 250 + 1000\bar{\varepsilon}^p$ MPa. The upper-die velocity is increased to 30 mm/s and the final compression is approximately 0.30 mm, corresponding to 1% engineering strain, so that the material passes through the elastic regime, initial yielding, and stable hardening.

As shown in Fig. 3(b), the solver enters the plastic regime near the theoretical yield strain of approximately 0.119%, with a yield-stress error of about 0.024%. The theoretical final stress is 258.72 MPa and the solver gives 258.77 MPa, corresponding to a final error of 0.019% and a mean path error of 0.025%. In Fig. 3(c), the equivalent plastic strain remains zero before yielding and then increases continuously. Its theoretical final value is 0.008718, compared with 0.008768 from the solver, giving a final error of 0.569% and a mean error of 0.511% over the plastic stage. Both stress and plastic strain evolve continuously without numerical jumps, showing that yield detection, plastic stress correction, and history-variable recursion operate stably within the explicit main loop.

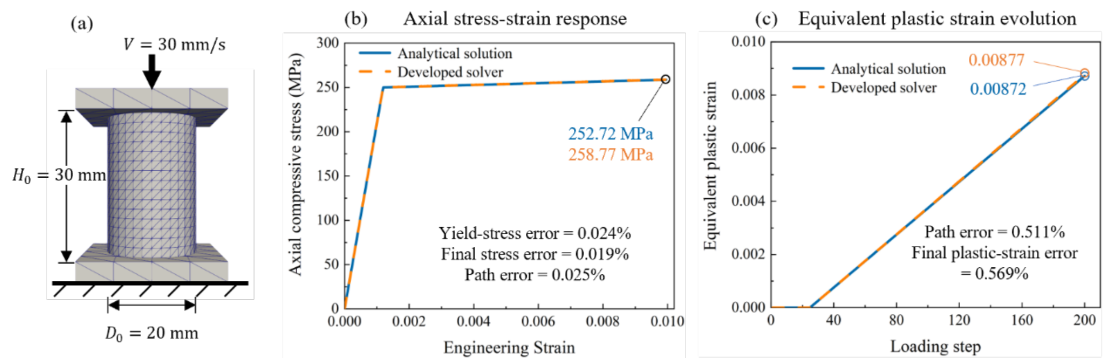

Fig.3 - Elastoplastic compression model, stress-strain response, and equivalent plastic strain evolution

Contact and forming-load verification

Contact and forming-load verification is performed by cylindrical upsetting. The initial dimensions are $D_0 = 20$ mm and $H_0 = 30$ mm. The workpiece is discretized with 10,080 tetrahedral elements, the upper and lower dies are treated as rigid bodies, and the Coulomb friction coefficient is $\mu = 0.12$. The total height reduction is 30%, giving a nominal final height of approximately 21 mm. Friction at the end faces restrains radial slip in the contact region and produces the characteristic barreled free surface, so that material flow, contact friction, and global reaction-force transfer can be examined simultaneously.

As shown in Fig. 4(a), the maximum mid-height diameter predicted by the developed solver is 22.43 mm, compared with 22.31 mm in the reference result, giving a relative error of approximately 0.54%. The end diameters are 20.46 and 20.35 mm, respectively, also differing by about 0.54%, while the final heights are

21.00 and 21.02 mm, corresponding to an error of about 0.10%. The two profiles agree closely at both the ends and the middle, indicating that the nonuniform radial flow induced by frictional constraint is reproduced with close agreement. In Fig. 4(b), the forming load increases continuously with stroke. The final/peak load is 278.70 kN for the developed solver and 276.19 kN for the reference calculation; the peak and final errors are both 0.91%, and the mean path error over the complete stroke is 1.07%. Simultaneous agreement in load trend and barreled geometry indicates a consistent overall response of constitutive hardening, contact-area growth, and frictional load transfer.

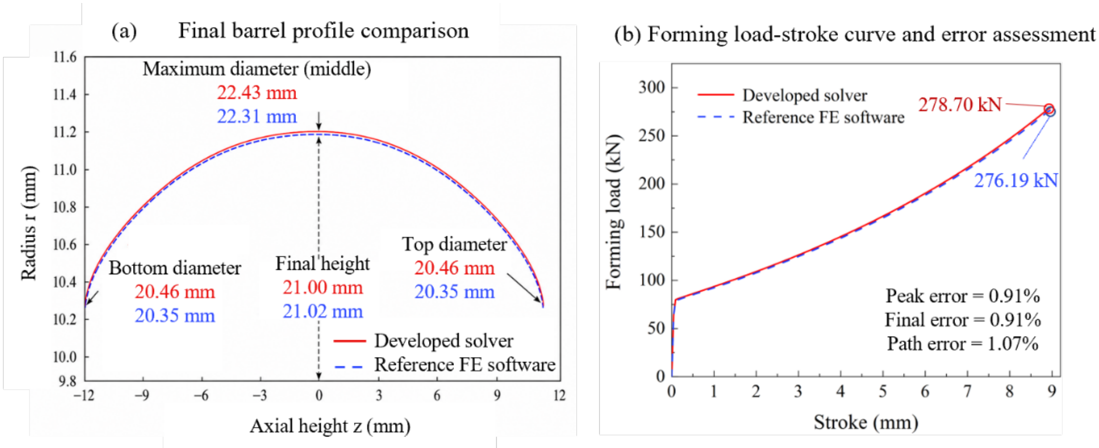

Fig.4 - Comparison of the final barrel profile and forming load-stroke response for cylindrical upsetting

Tab. 1 - Main quantitative results of the three-level verification

Verification item	Developed solver	Reference/analytical value	Relative error
Linear-elastic final stress	209.06 MPa	208.95 MPa	0.050%
Linear-elastic final reaction force	63.88 kN	65.64 kN	2.688%
Elastoplastic final stress	258.77 MPa	258.72 MPa	0.019%
Elastoplastic final plastic strain	0.008768	0.008718	0.569%
Upsetting maximum diameter	22.43 mm	22.31 mm	0.54%
Upsetting final height	21.00 mm	21.02 mm	0.10%
Upsetting peak load	278.70 kN	276.19 kN	0.91%

The three verification levels establish a continuous evidence chain from basic discretization through material nonlinearity to contact forming. The linear-elastic stress error is below 0.1%; the elastoplastic stress-path error is below 0.1%; the plastic-strain error is below 1%; and, in large-deformation upsetting with friction, the key geometric and load errors remain on the order of 1%. Within this verified scope, these results substantially reduce the likelihood that basic time-integration or constitutive-update errors dominate discrepancies in the subsequent application case, making geometry, mesh, and process settings the more relevant sources to examine.

RADIAL RING-ROLLING APPLICATION CASE

Model and loading conditions

To further examine solver applicability under large sliding on curved surfaces and moving contact, a three-dimensional TC4 radial ring-rolling case is selected as a complex application. Fig. 5(a) shows the overall finite element model, which consists of a deformable ring blank, main roll, mandrel, and auxiliary guide/conical rolls. The ring is discretized with four-node tetrahedral elements and all tools are treated as rigid bodies. The initial ring dimensions are$D_{\mathrm{out}} = 80$ mm, $D_{\mathrm{in}} = 40$ mm, and $H_0 = 16$ mm, and the mesh contains 4,911 nodes and 20,061 TETRA4 elements. As shown in Fig. 5(c), the main-roll angular velocity is $\omega = 0.60$ rad/s, while the Coulomb friction coefficients at the main-roll/ring and mandrel/ring interfaces are $\mu_{\mathrm{main}} = 0.30$ and $\mu_{\mathrm{mandrel}} = 0.04$, respectively. The mandrel is controlled by a segmented displacement history: an initial approach is followed by twelve smooth forming-feed increments, giving a total displacement of $1.05 + 12 \times 0.50 = 7.05$ mm. The mean radial velocity during the effective feed stage is approximately $v_r \approx 0.125$ mm/s. The larger friction on the main-roll side transfers tangential driving force, the mandrel primarily provides radial compression and wall-thickness control, and the auxiliary rolls restrain axial deviation and attitude instability. These loading conditions establish the basic force-transmission chain of main-roll rotation, radial mandrel reduction, and circumferential extension of the ring [13]-[16].

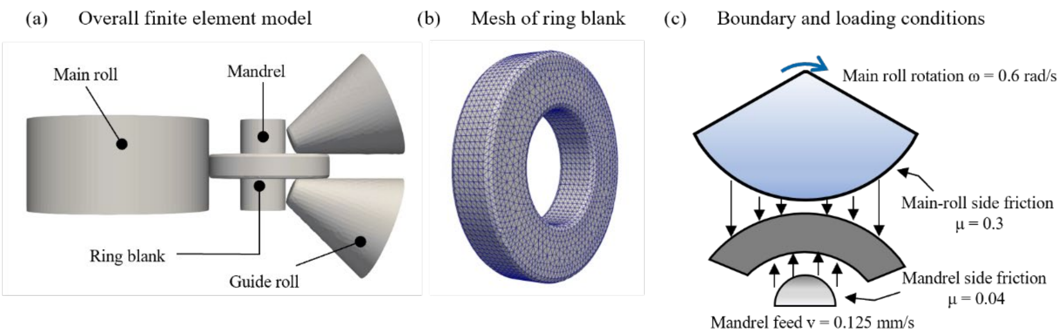

Fig.5 - Finite element model, ring-blank mesh, and boundary/loading conditions for radial ring rolling

Moving contact and equivalent-stress evolution

Unlike the relatively stationary contact region in cylindrical upsetting, the main-roll/ring and mandrel/ring contact patches in radial ring rolling continuously migrate along the outer and inner circumferential surfaces as the ring rotates. Fig. 6 shows the ring configuration and von Mises equivalent-stress distribution at the initial state, bite-in stage, intermediate rolling stage, and final forming state. The overall stress level is low initially. After mandrel feed begins, pronounced local stress concentrations first develop in the inner and outer contact regions, marking the establishment of stable bite-in and radial compressive loading. With continued main-roll driving, the wall thickness gradually decreases, the circumferential length increases, and the outer diameter expands. The high-stress regions migrate with the contact zones and redistribute circumferentially. By the final stage, the ring exhibits a clearly expanded configuration and a broader region of elevated equivalent stress, reflecting load transfer generated by the combined effects of continuous contact, frictional traction, and plastic flow.

Fig. 6 uses a common von Mises equivalent-stress color scale spanning approximately 1.9×10^1_3.4×10^2 MPa. From bite-in to final forming, both the configuration and stress field evolve continuously. Elevated stress is concentrated mainly around the instantaneous contact regions and neighboring material, and migrates with ring rotation rather than remaining fixed in space. This behavior requires the solver to update contact-candidate surfaces, normal relations, and friction states at every time step while continuously carrying material history variables with the material points. The results show that, with tetrahedral solid discretization and rigid tools, the unified explicit main loop can continuously handle moving contact in which radial reduction and tangential frictional driving coexist. The ring-rolling result in this section is intended to demonstrate application capability under a complex process condition rather than to provide an additional independent accuracy calibration. The quantitative accuracy conclusions of this paper therefore remain based on the analytical and same-condition reference finite element comparisons in Section 3. Temperature-related input in the ring-rolling case is excluded from the present mechanical-accuracy assessment; systematic thermo-mechanical coupling verification, remeshing, and parallel computation remain topics for future work.

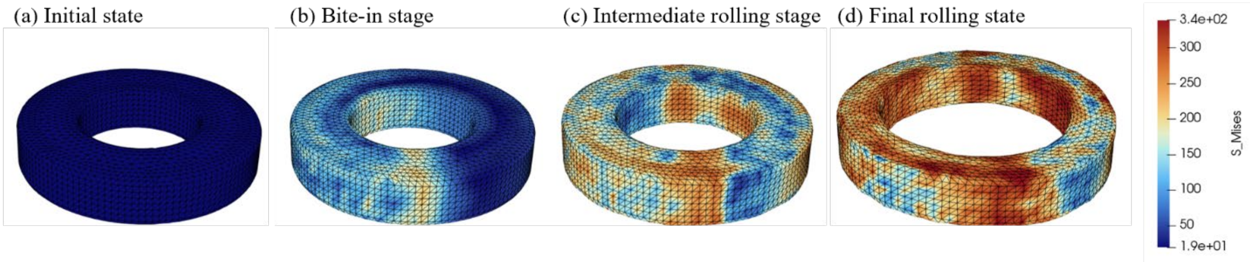

Fig.6 - Ring deformation and von Mises equivalent-stress evolution during radial ring rolling

CONCLUSIONS

1) A unified explicit finite element solution framework for forging simulation has been established. Lumped mass, central-difference time integration, constitutive integration, contact/friction treatment, and nodal motion are updated synchronously within the same step-by-step framework, and linear-elastic and elastoplastic analyses share one main solution loop.
2) In the linear-elastic verification, the final axial-stress error is 0.050% and the reaction-force error is 2.688%. In the elastoplastic verification, the final stress error is 0.019% and the final equivalent-plastic-strain error is 0.569%, demonstrating stable operation of the basic discretization and material-history update.
3) For cylindrical upsetting with a 30% reduction, the errors in maximum mid-height diameter, final height, and peak load are approximately 0.54%, 0.10%, and 0.91%, respectively, while the mean load-path error is 1.07%. The simultaneous agreement of the geometric profile and load history verifies the combined consistency of plastic flow, frictional contact, and global reaction-force transfer within the tested configuration.
4) The radial ring-rolling case further shows that the verified elastoplastic and contact mechanisms can be extended to continuously moving contact. Under main-roll rotation and radial mandrel feed, the ring progresses from bite-in to stable rolling with wall-thickness reduction, circumferential extension, and outer-diameter growth. Regions of high von Mises equivalent stress migrate with the contact zones and become more broadly distributed by the final stage. The quantitative conclusions of the present paper remain focused on explicit mechanical-solution accuracy; temperature-related input in the ring-rolling case is used only as part of the application condition, while systematic thermo-mechanical coupling verification, remeshing, and parallel computation are reserved for future work.

REFERENCES

[1] Taleb M, Husi G, Pálinkás S. Numerical simulation of die forging processes: a review of finite element modelling approaches, material models and process parameters. Appl Sci. 2026;16(14):6968.
[2] Zhang H, Tu H, Yuan C, et al. Predicting forging defects using FEM: a brief review. Int J Adv Manuf Technol. 2025;141(3-4):1143-57.
[3] Dourandish S, Champliaud H, Morin J-B, et al. Numerical simulation and experimental validation of microstructure evolution during the upsetting process of a large size martensitic stainless steel forging. Int J Mater Form. 2024;17:38.
[4] Obiko J, Shongwe MB, Malatji N. On the effect of deformation conditions on the metal flow behavior during upsetting process using finite element simulation. Int J Interact Des Manuf. 2025;19:4225-41.
[5] Dixit US, Raja A, Petrov PA, Matveev AG. Numerical simulations for studying the influence of friction in forging. Adv Mater Process Technol. 2022;8(3):2752-74.
[6] Li Q-M, Yi Z-W, Liu Y-Q, et al. Explicit analysis of sheet metal forming processes using solid-shell elements. Metals. 2022;12(1):52.
[7] Ozgeneci Z, Music O, Şimşir C. Finite element analysis of damage in hot forging of bearing rings. Int

J Adv Manuf Technol. 2025;137(1):891-911.
[8] Han B, Kim K, Park J, et al. Preform design to reduce forging load and grain size simultaneously in disk forging of IN718. J Mater Res Technol. 2024;31:1644-54.
[9] Sahu I, Petrinic N. Unbiased higher-order frictional contact using midplane and patch based segment-to-segment penalty method. Comput Mech. 2026;77:1635-59.
[10] Chu D, Rong Y, Zhou Z, et al. Robust explicit computational strategies based on penalty method for large-deformation impact problems. Explosion and Shock Waves. 2025;45(3):034201.
[11] Li Y, Xu J, Liu Y, et al. MPI/OpenMP-based parallel solver for imprint forming simulation. Comput Model Eng Sci. 2024;140(1):461-83.
[12] Bodunrin M, Obiko J, Klenam D. On the uniaxial compression testing of metallic alloys at high strain rates: an assessment of DEFORM-3D simulation. Appl Sci. 2023;13(4):2686.
[13] Hua L, Qian D, Deng J, et al. Theory and technology of super-large ring rolling. Forging & Stamping Technology. 2018;43(7):17-31. [in Chinese].
[14] Lan J, Qian D, Deng J, Hua L. Development of green and intelligent rolling for high performance ring parts. Journal of Mechanical Engineering. 2022;58(20):186-97. doi:10.3901/JME.2022.20.186. [in Chinese].
[15] Li L, Yang H, Guo L, Sun Z. A control method of guide rolls in 3D-FE simulation of ring rolling. J Mater Process Technol. 2008;205(1-3):99-110.
[16] Xu SG, Weinmann KJ, Yang DY, Lian JC. Simulation of the hot ring rolling process by using a thermo-coupled three-dimensional rigid-viscoplastic finite element method. J Manuf Sci Eng. 1997;119(4A):542-9.